A WEAK DISPERSION 3D WAVE FIELD SIMULATION METHOD: A PREDICTOR-CORRECTOR METHOD OF THE IMPLICIT RUNGE-KUTTA SCHEME

NIAN WANG[1] and YANJIE ZHOU[1,2]

[1] Department of Mathematical Sciences, Tsinghua University, Beijing 100084, P.R. China. happyxiaoxi114@163.com
[2] Department of Mathematics, School of Science, Beijing Technology and Business University (BTBU), Beijing 100048, P.R. China.

ABSTRACT

Wang, N. and Zhou, Y., 2014. A weak dispersion 3D wave field simulation method: A predictor-corrector method of the implicit Runge-Kutta scheme. *Journal of Seismic Exploration*, 23: 431-462.

We propose a numerical method for solving the acoustic- and elastic-wave equations, which is called the predictor-corrector method of the implicit Runge-Kutta scheme (IRK-PCM). This work is an extension of the corresponding 2D IRK-PCM to the 3D case. To solve wave equations, we first transform them into a system of semi-discrete ordinary differential equations (ODEs). And then we use the local interpolation theory for spatial discretization, and use the 2-step predictor-corrector method based on an implicit Runge-Kutta method for the temporal discretization. In this paper, we investigate the theoretical property of the 3D IRK-PCM including stability criteria, approximation error, numerical dispersion, and computational efficiency when solving the acoustic wave equation. Seismic wave field simulations for both acoustic and elastic models show that the 3D IRK-PCM can suppress effectively the numerical dispersion caused by the discretization of wave equations when coarse grids are used, high frequency bands are chosen, or models have large velocity contrasts between adjacent layers. Whereas other high-order schemes such as the fourth-order LWC and the staggered-grid (SG) method suffer from serious numerical dispersion for the same cases. It suggests that to achieve the same accuracy, the 3D IRK-PCM can increase greatly the computational speed and save significantly the storage space. We conclude that the IRK-PCM provides us an useful tool for the 3D large-scale wave field simulation, reverse time migration and full waveform inversion.

KEY WORDS: wave equation, wave-field simulation, numerical dispersion, implicit Runge-Kutta method, predictor-corrector method, anisotropy, shear wave splitting.

INTRODUCTION

Numerical methods always play an important role in seismic exploration whether for forward modeling of seismic wave fields in complex media or for solving inverse problems. Many methods have been developed and applied in the 3D isotropic and anisotropic problems. Finite-difference (FD) methods for solving wave equations provide us useful tools in exploration seismology, however, they meet bottleneck for their costly central processing unit (CPU) time and large amounts of direct-access memory or seriously numerical dispersion, when too few samples per wavelength are used or models have large velocity contrasts between adjacent layers. In order to break the bottleneck of the FD methods when applying in large-scale wave-field modeling, one way is to use the high-order finite-difference (FD) methods (Lax and Wendroff, 1964; Kelly et al., 1976; Dablain, 1986; Takeuchi and Geller, 2000; and many others) such as high-order compact FD scheme including the so-called Lax-Wendroff correction (LWC) scheme (Lax and Wendroff, 1964; Dablain, 1986) and the staggered-grid FD method (Virieux, 1986; Fornberg, 1990). However, the numerical dispersion also affects the performance of the high-order difference methods especially when too-coarse grids or too few samples per wavelength are used. In other words, the high-order FDs also suffer from the numerical dispersion (Wang et al., 2002). Moreover, the high-order FDs demand more grids in a spatial direction, resulting in difficulties in efficient parallel computation and the implementation of the absorbing boundary condition.

The finite element method (FEM) (Turner et al., 1956; Whiteman, 1975; Ciarlet, 1978; Johnson, 1990; Eriksson and Johnson, 1991; Solin et al., 2003; Yang et al., 2008) is a variational method which can flexibly handle complex topography and boundary conditions, but it needs to solve a system of linear equations whose mass matrices are of wide bandwidths, resulting in large space storage and computational CPU time especially when applied to the 3D wave propagation modeling. The spectral method which uses a global basis has a good property called exponential "convergence", but it involves the fast Fourier transform (FFT) which is time consuming. Meanwhile, the spectral method also has the numerical dispersion in time (Gottlieb and Orzag, 1977). The spectral-element method (SEM) (Komatitsch and Vilotte, 1998; Komatitsch et al., 2000) solves the partial differential equation in a frame of finite element method, and combined with a high accuracy of spectral techniques. Though it uses some diagonally techniques such as orthogonal polynomial basis, the SEM cannot avoid solving linear equation. So the computational time should be taken into consideration especially when it applied to the 3D case.

The flux-corrected transport (FCT) technique (Fei and Larner, 1995; Zhang et al., 1999; Yang et al., 2002; Zheng et al., 2006) can effectively suppress the numerical dispersion caused by discretizing wave equations, but it is unable to fully recover the resolution lost by eliminating the numerical

dispersion when the spatial sampling becomes too coarse (Yang et al., 2002). The so-called "nearly analytic discrete method (NADM)" and its improved algorithms were suggested by Yang et al. for reducing the numerical dispersion caused by the discretization of acoustic- and elastic-wave equations for both 2D and 3D cases (2003, 2007, 2010). These methods use the wave displacement-, the particle velocity- and their gradient-fields simultaneously to reconstruct the wave displacement-fields, and they are able to suppress the numerical dispersions effectively. The weak numerical dispersion NAD methods or its modified NAD methods are also extended to porous media (Yang et al., 2007, 2014). Meanwhile, they are combined with different time advancing algorithms such as the explicit Runge-Kutta method (Chen et al., 2010), implicit Runge-Kutta method (Yang et al., 2009; Wang et al., 2010), implicit multi-step Adams method (Yang and Wang, 2010), and the symplectically partitioned Runge-Kutta method (Ma et al., 2011, 2014) for solving isotropic and anisotropic wave equations.

The main purpose of this paper is to present the 3D predictor-corrector method (IRK-PCM) which can effectively suppressing the numerical dispersion for modeling wave propagating in both isotropic and anisotropic media even by using large grid steps. It is actually an extension of the 2D IRK-PCM (Wang et al., 2012) for solving the acoustic- and elastic-wave equations for the 3D case. We first transform the wave equation into a system of semi-discrete ordinary differential equations (ODEs). And then we use the explicit IRK-PCM based on an implicit Runge-Kutta method to solve the obtained semi-discrete ODEs. To verify the numerical error behavior of the 3D IRK-PCM, we compare the numerical error of the 3D IRK-PCM with those of the second-order conventional FD scheme and the fourth-order LWC method for the 3D initially value problem of the acoustic wave equation, measured quantitatively by the root-mean-square deviation from the analytical solution. Meanwhile, we analyse the numerical dispersion and stability condition of the IRK-PCM, compare waveforms computed by the 3D IRK-PCM with the analytical solutions, and present some seismic wave field snapshots in 3D multi-layer acoustic layers, isotropic and transversely isotropic elastic media.

PREDICTOR-CORRECTOR METHOD BASED ON THE IMPLICIT RUNGE-KUTTA SCHEME

Transform of wave equations

In a heterogeneous elastic medium, the wave equation can be written as

$$\rho(\partial^2 U/\partial t^2) = \nabla \cdot \sigma + f$$
$$\sigma = C:\varepsilon \qquad , \qquad (1)$$
$$\varepsilon = \tfrac{1}{2}[\nabla U + (\nabla U)^T]$$

where ρ denotes the density, $U = (u_1, u_2, u_3)^T$ the displacement vector, σ and ε the second-order symmetric stress and the strain tensor, respectively, C the fourth-order stiffness tensor, and $f = (f_1, f_2, f_3)^T$ the external source force.

We can rewrite eq. (1) as follows

$$\rho(\partial^2 U/\partial t^2) = D \cdot U + f \; , \tag{2}$$

where D is the second-order partial differential operator. For example, for the 3D homogeneous acoustic equation

$$\partial^2 u/\partial t^2 = c^2[(\partial^2 u/\partial x^2) + (\partial^2 u/\partial y^2) + (\partial^2 u/\partial z^2)] + f \; , \tag{3}$$

eq. (3) can be written as follows

$$\partial^2 u/\partial t^2 = D \cdot u + f \; ,$$
where

$$D = c^2[(\partial^2/\partial x^2) + (\partial^2/\partial y^2) + (\partial^2/\partial z^2)] \; ,$$

in which c is the wave velocity.

Let $W = \partial U/\partial t = [(\partial u_1/\partial t), (\partial u_2/\partial t), (\partial u_3/\partial t)]^T$, then eq. (2) can be written as

$$\partial U/\partial t = W \; ,$$
$$\partial W/\partial t = (1/\rho)D \cdot U + (1/\rho)f \; . \tag{4}$$

Let $V = (U \cdot W)^T$, then eq. (4) can further be written as

$$\partial V/\partial t = L \cdot V + F \; , \tag{5}$$

where

$$L = \begin{bmatrix} 0 & I \\ (1/\rho)D & 0 \end{bmatrix}, \quad F = \begin{pmatrix} 0 \\ (1/\rho)f \end{pmatrix} \; .$$

From eq. (4), we have the following equations:

$$\partial^2 V/\partial t \partial x = L \cdot V_x + F_x \; ,$$
$$\partial^2 V/\partial t \partial y = L \cdot V_y + F_y \; , \tag{6}$$
$$\partial^2 V/\partial t \partial z = L \cdot V_z + F_z \; ,$$

where $V_x = \partial V / \partial x$, $V_y = \partial V / \partial y$ and $V_z = \partial V / \partial z$.

Let

$$\bar{V} = (V, V_x, V_y, V_z)^T, \quad \bar{F} = (F, F_x, F_y, F_z)^T, \quad \text{and} \quad \bar{L} = \text{diag}(L, L, L, L),$$

then we have the following vector equation, from eqs. (5) and (6),

$$\partial \bar{V} / \partial t = \bar{L} \cdot \bar{V} + \bar{F} \ . \tag{7}$$

Formulation of the IRK-PCM

Owing to the local elastic property of rocks, we use the local interpolation method (Kondoh et al., 1994; Yang and Wang, 2010) to approximate the high-order derivatives $(\partial^{k+l+m} U / \partial x^k \partial y^l \partial z^m)^n_{i,j,k}$ and $(\partial^{k+l+m} W / \partial x^k \partial y^l \partial z^m)^n_{i,j,k}$ ($2 \leq k+l+m \leq 3$) included in the right-hand side of (7) through using the values of the wave displacement, the particle-velocity, and their gradients at the grid point (i, j, k) and its neighboring grid points. These computational formulae of approximating the second- and third-order derivatives are listed in Appendix A. In this case of discretizing the high-order spatial derivatives on the right-hand side of eq. (7), this equation enters into a semi-discrete ODE system.

For the temporal discretization, similar to the 2D case (Wang et al., 2012), we use the implicit Runge-Kutta method combined with the predictor-corrector algorithm. The diagonal implicit Runge-Kutta method to solve the semi-discrete ODEs (7) is as follows (Hairer et al., 1993)

$$\bar{V}^{n+1}_{i,j,k} = \bar{V}^n_{i,j,k} + (\Delta t / 2)(K^n_{i,j,k} + \bar{K}^n_{i,j,k}) \ , \tag{8}$$

$$K^n_{i,j,k} = \bar{L}(\bar{V}^n_{i,j,k} + r\Delta t K^n_{i,j,k}) + F_{i,j,k}(t_n + r\Delta t) \ , \tag{9}$$

$$\bar{K}^n_{i,j,k} = \bar{L}[\bar{V}^n_{i,j,k} + (1-2r)\Delta t K^n_{i,j,k} + r\Delta t \bar{K}^n_{i,j,k}] + F_{i,j,k}[(t_n + (1-r)\Delta t] \ , \tag{10}$$

where $r = (1/2) - (\sqrt{3}/6)$.

Obviously, if using the algorithms (8)-(10) directly to compute the wave-displacement and its gradients, we need to solve two systems of linear algebraic eqs. (9) and (10) at each step of time advancing, resulting in great increase of the computational cost. To avoid solving the system of linear equations caused by using the implicit method, in the following we try to change the implicit method into an explicit predictor-corrector algorithm (IRK-PCM). In detail, the 2-step explicit IRK-PCM is presented as follows (Yang et al., 2012; Wang et al., 2012):

Predictor:

$$K_{i,j,k}^{n}{}^{(1)} = \bar{L}\bar{V}_{i,j,k}^{n} \ , \tag{11}$$

Corrector:

$$K_{i,j,k}^{n}{}^{(2)} = K_{i,j,k}^{n}{}^{(1)} + r\Delta t\bar{L}K_{i,j,k}^{n}{}^{(1)}$$

$$= \bar{L}\bar{V}_{i,j,k}^{n} + r\Delta t\bar{L}^{2}\bar{V}_{i,j,k}^{n} \ , \tag{12}$$

$$K_{i,j,k}^{n} = K_{i,j,k}^{n}{}^{(2)} + r\Delta t\bar{L}K_{i,j,k}^{n}{}^{(2)} + F_{i,j,k}(t_{n} + r\Delta t)$$

$$= \bar{L}\bar{V}_{i,j,k}^{n} + 2r\Delta t\bar{L}^{2}\cdot\bar{V}_{i,j,k}^{n} + (r\Delta t)^{2}\bar{L}^{3}\cdot\bar{V}_{i,j,k}^{n} + F_{i,j,k}(t_{n} + r\Delta t) \ , \tag{13}$$

where the second-order operator $\bar{L}^{2}$ can be obtained from definition of $\bar{L}$ as follows

$$\bar{L}^{2} = \text{Diag}(L^{2},L^{2},L^{2},L^{2})$$

$$= \text{Diag}[(1/\rho)D,(1/\rho)D,(1/\rho)D,(1/\rho)D,(1/\rho)D,(1/\rho)D,(1/\rho)D]. \tag{14}$$

Similarly, we can obtain the following approximation, deriving from eq. (10),

$$\bar{K}_{i,j,k}^{n} = \bar{K}_{i,j,k}^{n}{}^{(1)} + r\Delta t\bar{L}\cdot\bar{K}_{i,j,k}^{n}{}^{(1)} + F_{i,j,k}[t_{n} + (1-r)\Delta t]$$

$$= \bar{L}\bar{W}_{i,j,k}^{n} + 2r\Delta t\bar{L}^{2}\cdot\bar{W}_{i,j,k}^{n} + (r\Delta t)^{2}\bar{L}^{3}\cdot\bar{W}_{i,j,k}^{n} + F_{i,j,k}[t_{n} + (1-r)\Delta t] \ , \tag{15}$$

where $\bar{K}_{i,j,k}^{n} = \bar{L}\bar{W}_{i,j,k}^{n} + r\Delta t\bar{L}^{2}\cdot\bar{W}_{i,j,k}^{n}$. $\bar{W}_{i,j,k}^{n} = \bar{V}_{i,j,k}^{n} + (1-2r)\Delta tK_{i,j,k}^{n}$.

Combining eq. (8) with eqs. (13) and (15), we obtain the explicit IRK-PCM for solving the wave eqs.. For practical calculations, the implementation of the IRK-PCM is divided into three major steps. The computational steps are described below

1. Computing $K_{i,j,k}^{n}$ using eqs. (11)-(13).

(a) Using formulae (A-1) to (A-5) to compute $\bar{L}\bar{V}_{i,j,k}^{n}$ and $\bar{L}^{2}\bar{V}_{i,j,k}^{n}$, then substituting them into eq. (12) to obtain $K_{i,j,k}^{n}{}^{(2)}$;

(b) Using the obtained result $K_{i,j,k}^{n}{}^{(2)}$ in the first step (a) and applying the similar computational formulae as (A-1) and (A-5) to compute $\bar{L}K_{i,j,k}^{n}{}^{(2)}$;

(c) Substituting these results obtained in steps (a) and (b) into eq. (13) to obtain $K_{i,j,k}^{n}$.

2. Computing $\bar{K}^n_{i,j,k}$ through using eq. (15). In this step, we use the similar steps to computing $K^n_{i,j,k}$ in the first step to obtain $\bar{K}^n_{i,j,k}$. The difference is that these vectors $V^n_{i,j,k}$ and $K^n_{i,j,k}{}^{(2)}$ in computing $K^n_{i,j,k}$ are replaced by the vectors $W^n_{i,j,k}$ and $\bar{K}^n_{i,j,k}{}^{(1)}$ when computing $\bar{K}^n_{i,j,k}$;

3. Substituting these obtained results $K^n_{i,j,k}$ and $\bar{K}^n_{i,j,k}$ into eq. (8) to obtain the values of $\bar{V}^{n+1}_{i,j,k}$ at the (n+1)-th time level.

Note that the fourth-terms at the right-hand side of eqs. (13) and (15) can be easily computed because of the known analytical source function F.

ERROR ANALYSIS

Theoretical analysis

Using the Taylor series expansion, we can obtain that the errors of $(\partial^{k+l+m}\bar{V}/\partial x^k \partial y^l \partial z^m)^n_{i,j}$, $(2 \le k+l+m \le 3)$ are $O(\Delta x^4 + \Delta y^4 + \Delta z^4)$ caused by the interpolation approximations presented in Appendix A. Due to using the third-order implicit Runge-Kutta method and the predictor-corrector method to solve the semi-discrete ODEs (7), the temporal error, caused by the discretization of the temporal partial derivative, is $O(\Delta t^2)$. Therefore, the error introduced by the IRK-PCM is $O(\Delta t^2 + \Delta x^4 + \Delta y^4 + \Delta z^4)$. In other words, the 3D IRK-PCM suggested in this paper has a fourth-order accuracy in space and second-order accuracy in time.

Numerical analysis

To further illustrate the accuracy of our present method, in the following we compare the numerical errors caused by the IRK-PCM against other methods such as the conventional second-order FD and the fourth-order LWC methods for the 3D acoustic wave equation. Consider the following 3D initial value problem

$$\partial^2 u/\partial t^2 = c^2[(\partial^2 u/\partial x^2) + (\partial^2 u/\partial y^2) + (\partial^2 u/\partial z^2)] \ , \tag{16a}$$

$$u(0,x,y,z) = \cos[-(2\pi f_0/c)(l_0 \cdot x + m_0 \cdot y + n_0 \cdot z)] \ , \tag{16b}$$

and

$$\partial u(0,x,y,z)/\partial t = -2\pi f_0 \sin[-(2\pi f_0/c)(l_0 \cdot x + m_0 \cdot y + n_0 \cdot z)] \ , \tag{16c}$$

where f_0 denotes the frequency, c is the wave velocity, and the vector (l_0, m_0, n_0) is the direction of the incident acoustic wave at the time $t = 0$ s, which is chosen by $(l_0, m_0, n_0) = [(1/\sqrt{3}),(1/\sqrt{3}),(1/\sqrt{3})]$ in the experiment.

Obviously, the analytical solution for the initial value problem (16) is

$$u(t,x,y,z) = \cos\{2\pi f_0[t - l_0 \cdot (x/c) - m_0 \cdot (y/c) - n_0 \cdot (z/c)]\} \ .$$

In this numerical experiment, we choose the number of grid points , the peak frequency Hz, the velocity . The relative error () for the 3D case is defined as follows (Konddoh et al., 1994)

$$E_r(\%) = [\sum_{i=1}^{N} \sum_{j=1}^{N} \sum_{k=1}^{N} [u_{i,j,k}^n - u(t_n,x_i,y_j,z_k)]^2$$

$$/ \sum_{i=1}^{N} \sum_{j=1}^{N} \sum_{k=1}^{N} [u(t_n,x_i,y_j,z_k)]^2]^{1/2} \times 100 \ , \tag{17}$$

where $u_{i,j,k}^n$ is the numerical solution and $u(t_n,x_i,y_j,z_k)$ is the analytical solution of the initial value problem.

Figs. 1, 2 and 3 plot the relative errors E_r versus time for different spatial and temporal increments shown in a semi-log scale, where three lines of E_r corresponding to the IRK-PCM, the fourth-order LWC method, and the second-order FDM. In these figures, the maximum relative errors for different cases are listed in Table 1. From these error curves and Table 1 ($\Delta x = \Delta y = \Delta z = h$), we find that for the fixed time step, when the spatial step is relatively small, the relative error E_r of the IRK-PCM is bigger than that of the fourth-order LWC method and is less than that of the second-order FDM (see Fig. 1). As the spatial step increases, the relative error of the IRK-PCM is smaller than those of both the fourth-order LWC method and the second-order FDM (see Figs. 2 and 3).

Table 1. Comparison of maximum E_r (%) for different cases and different methods.

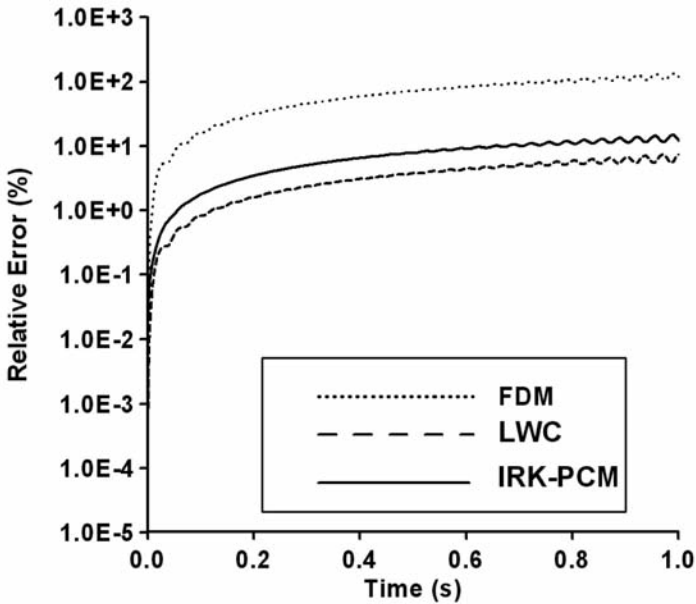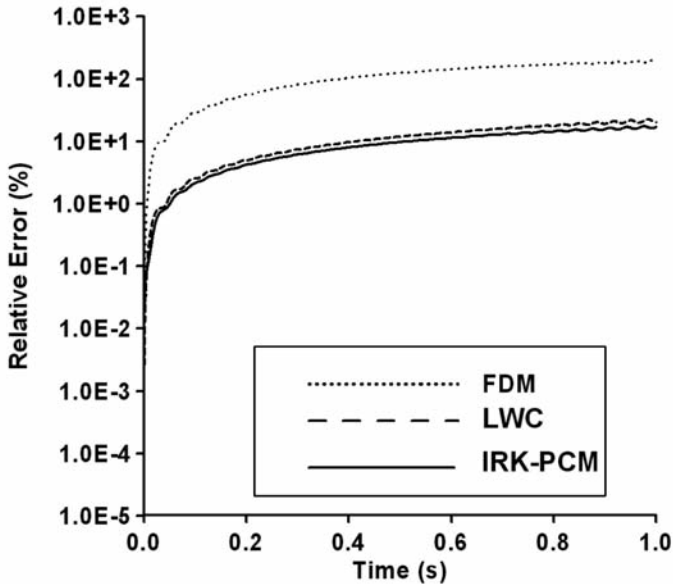| Methods	Second-order FDM	Fourth-order LWC	IRK-PCM
Case 1:	h = 30 m $\Delta t = 1 \times 10^{-4}$ s	134.633	7.46825	14.8178
Case 2:	h = 40 m $\Delta t = 1 \times 10^{-4}$ s	197.549	22.42	17.4703
Case 3:	h = 50 m $\Delta t = 1 \times 10^{-4}$ s	204.629	53.7422	34.6667

Fig. 1. The relative errors of the IRK-PCM, the fourth-order LWC method, and the second-order FDM measured by E_r [formula (17)] are shown in a semi-log scale for the 3D initial value problem (16). The spatial and the temporal increments are 30 m and 1×10^{-4} s, respectively.
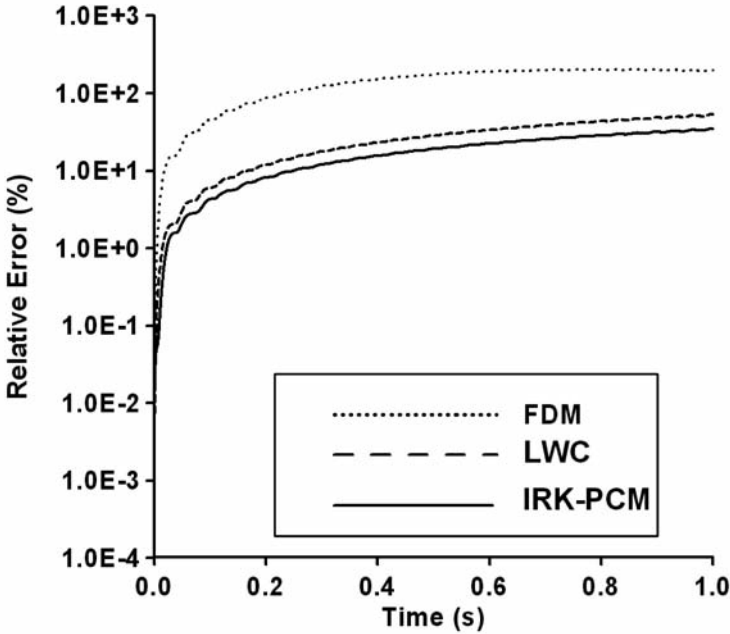

Fig. 2. The relative errors of the IRK-PCM, the fourth-order LWC method, and the second-order FDM measured by E_r [formula (17)] are shown in a semi-log scale for the 3D initial value problem (16). The spatial and the temporal increments are 40 m and 1×10^{-4} s, respectively.

Fig. 3. The relative errors of the IRK-PCM, the fourth-order LWC method, and the second-order FDM measured by E_r [formula (17)] are shown in a semi-log scale for the 3D initial value problem (16). The spatial and the temporal increments are 50 m and 1×10^{-4} s, respectively.

STABILITY OF THE 3D IRK-PCM

It is well known that the temporal increment, the spatial increment, and the wave velocity must satisfy certain relationship to keep numerical calculation stable. In this section, through the Fourier analyses (Richtmyer and Morton, 1967; Guan and Lu, 2006), we obtain the stability criterion of the IRK-PCM for the 3D case. The algebraic details for the stability of the 3D IRK-PCM are discussed in Appendix B, and here we only give the stability condition under the condition of $\Delta x = \Delta y = \Delta z = h$ as follows

$$c(\Delta t/h) \leq \alpha_{max} \leq 0.505 \ , \tag{18}$$

or

$$\Delta t \leq 0.505(h/c) \ , \tag{19}$$

where α_{max} denotes the maximum value of the Courant number defined by $\alpha = c\Delta t/h$ (Sei and Symes, 1994; Dablain, 1986) in which Δt is the temporal step size and h is the spatial step size.

When the 3D IRK-PCM is applied to solve the 3D anisotropic elastic-wave equation, we roughly estimate that the temporal increment should satisfy the following stability condition

$$\Delta t \leq \Delta t_{max} \approx 0.505(h/c_{max}) \ , \tag{20}$$

where Δt_{max} denotes the maximum temporal increment and c_{max} is the maximum P-wave velocity.

NUMERICAL DISPERSION OF THE 3D IRK-PCM

Fig. 4 shows the numerical dispersion curves as a function of the spatial sampling ratio Sp $= h/\lambda$ (Moczo et al., 2000), computed by the IRK-PCM for the acoustic wave equation at different propagation angles with respect to the x-axis (δ_1) and z-axis (δ_2). The symbol R is defined as the ratio of numerical phase velocity to the real phase velocity ($R = c_{num}/c_0$). The 3D IRK-PCM introduces no numerical dispersion when R is equal to one; whereas it suffers from different amount of numerical dispersions when R is different from one. The details of the dispersion analysis are discussed in Appendix C. In Figs. 4a-d, the Courant number α is fixed at 0.1, where the four lines correspond to when δ_1 or δ_2 is fixed, the other angle changes from 0°, 15°, 30°, and 45°. We find in Fig. 4a where $\delta_1 = 0$ that when the sampling ratio Sp $\in$ [0.3 0.45], the 3D IRK-PCM suppress numerical dispersions better as δ_2 increases; whereas as the sampling ratio tends to 0.5 (2 points per wavelength are used), the 3D IRK-PCM suppress numerical dispersion better when $\delta_2 = 30°$ than that when $\delta_2 = 45°$. In other cases (see Figs. 4c-d), when δ_1 or δ_2 is fixed, the 3D IRK-PCM suppress numerical dispersions better as the other angle increases when Sp $\in$ [0.3 0.5]. But it is shown in the four cases (Fig. 4) that the maximum deviation of the numerical velocity from the exact one is within 2% even when about 3 points per wavelength are used (Sp $\approx$ 0.3).

Fig. 5 shows the numerical dispersion curves of the 3D IRK-PCM as a function of the sampling ratio Sp $= h/\lambda$ for solving the homogeneous acoustic wave equation when the propagation angles δ_1 and δ_2 are fixed, where the four lines correspond to when the courant number α changes from 0.1, 0.2, 0.3, and 0.4. We see that R increases as α increases when the sampling ratio S $\in$ [0.3 0.5], which means the courant number α too small or too large is not good for suppressing numerical dispersion in practical use of the 3D IRK-PCM. Also, we find that the maximum deviation of the numerical velocity from the exact one is within 2% even when about 3 points per wavelength are used (Sp $\approx$ 0.3) and $\alpha \in$ [0.1 0.4].
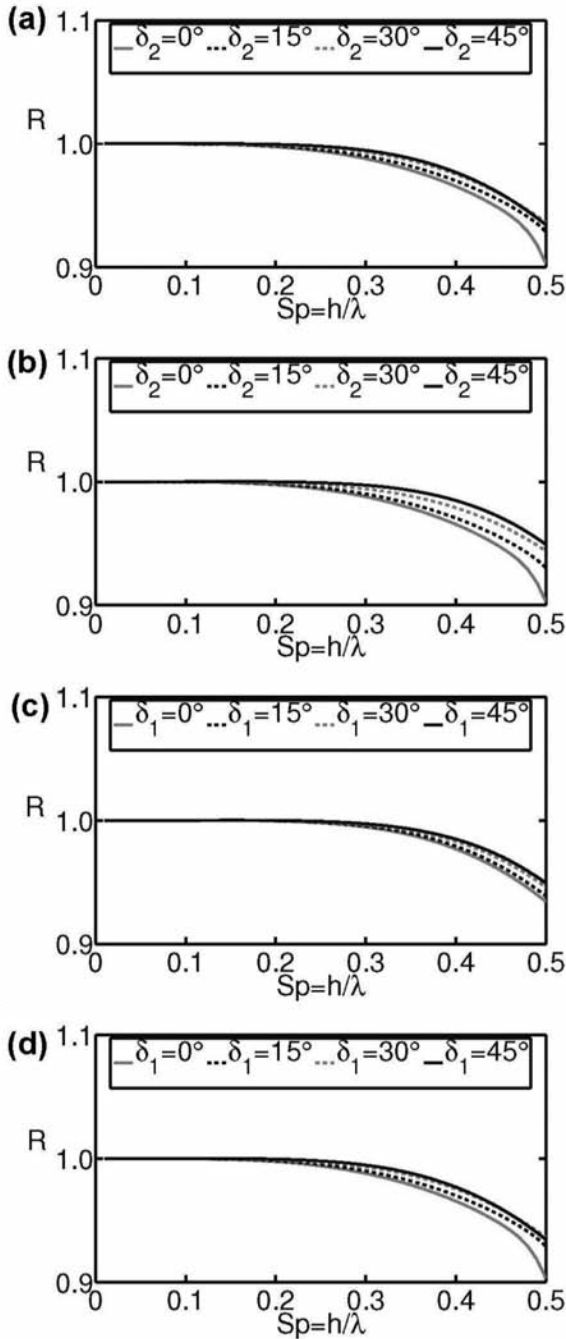
Fig. 4. The ratio R of the numerical velocity (c_{num}) to the exact phase velocity (c_0) versus the spatial sampling ratio $S = h/\lambda$, generated by the IRK-PCM under the courant number $\alpha = 0.1$ and at different wave propagation angles with respect to the x-axis (δ_1) or the z-axis (δ_2). Where the four lines correspond to when (a) $\delta_1 = 0°$, (b) $\delta_1 = 45°$, (c) $\delta_2 = 45°$, (d) $\delta_2 = 90°$ is fixed, and the other angle changes from 0°, 15°, 30°, and 45°, respectively.
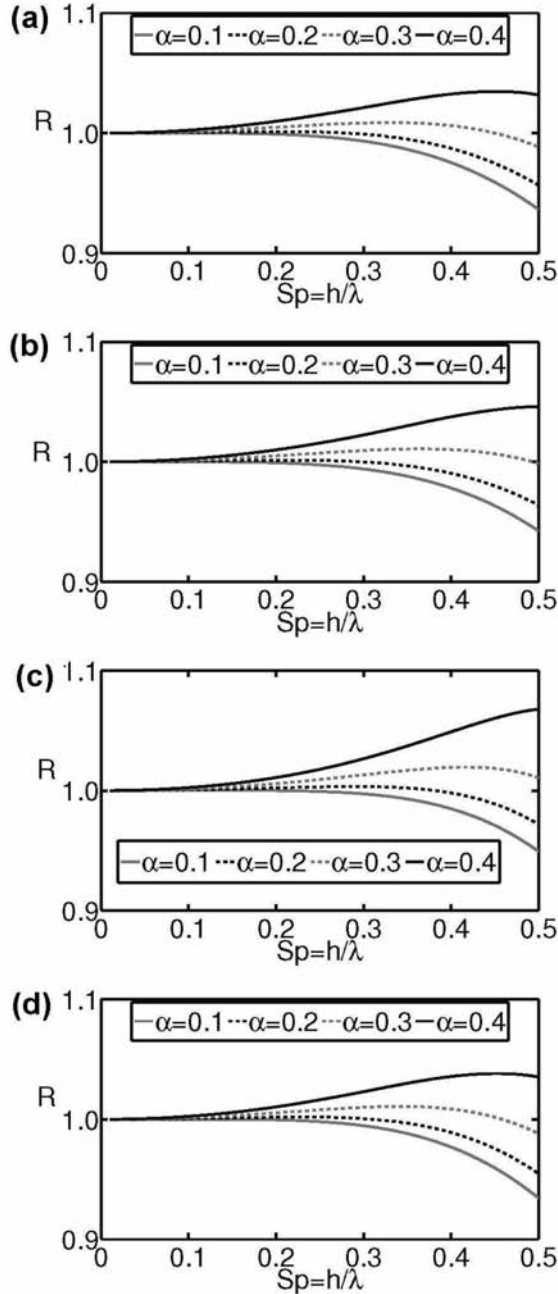
Fig. 5. The ratio R of the numerical velocity (c_{num}) to the exact phase velocity (c_0) versus the sampling ratio $S = h/\lambda$, generated by the IRK-PCM at different courant number when wave propagation angles with respect to the x-axis (δ_1) and the z-axis (δ_2) are fixed. Where the four lines correspond to when (a) $\delta_1 = 0°$, $\delta_2 = 30°$, (b) $\delta_1 = 30°$, $\delta_2 = 30°$, (c) $\delta_1 = 45°$, $\delta_2 = 45°$, (d) $\delta_1 = 45°$, $\delta_2 = 90°$ are fixed, and the courant number α changes from 0.1, 0.2, 0.3 and 0.4, respectively.

EFFICIENCY AND WAVE FIELD MODELING

In this section, we investigate the efficiency of the IRK-PCM for wave-field modeling in the 3D acoustic, isotropic and transversely isotropic elastic cases, and compare it against the fourth-order LWC method (Dablain, 1986) and the fourth-order staggered-grid (SG) FD method (Virieux, 1986). Different spatial sampling rates are chosen so that we test the effects of sampling rate, which is defined by

$$\Delta x = v_{min}/f \cdot G = \lambda_{min}/G \quad, \tag{21}$$

where v_{min} denotes the minimum S-wave (or quasi S-wave) velocity, f is the peak frequency, and G denotes the number of grid points per minimum wavelength ($G = \lambda_{min}/\Delta x$). All of our numerical experiments were performed on an Intel(R) Xeon(R) CPU with 2.60 GHz and 64 GB memory.

Computational efficiency

To examine the efficiency of the IRK-PCM, we solve numerically the 3D acoustic wave eq. (3) given previously. In this experiment, we choose the computational domain of $0 < x \leq 4.8$ km, $0 < y \leq 4.8$ km, $0 < z \leq 4.8$ km, the acoustic velocity of $c_0 = 3400$ m/s. The time and spatial increments are respectively $\Delta t = 0.0025$ s and $\Delta x = \Delta y = \Delta z = 48$ m, resulting in $G \approx 3.5$. The receiver R is at the grid point (2.4 km, 2.4 km, 2.4 km). The number of grid points is $101 \times 101 \times 101$ and the force source f is a Ricker wavelet (Zahradnik et al., 1993)

$$f(t) = \sin(2\pi f_0 t)\exp(-4\pi^2 f_0^2 t^2/16) \quad, \tag{22}$$

with a peak frequency of $f_0 = 20$ Hz, and is located at the center of the computational domain.

Fig. 6 shows the snapshots of seismic wave fields at t = 0.5 s in the x-y plane, generated by the IRK-PCM, the fourth-order LWC, and the fourth-order SG method, respectively. From Fig. 6 we can see that the wave-fronts of seismic waves simulated by the three methods at the same time are basically identical, and it took the IRK-PCM, the fourth-order LWC, and the SG about 166 s, 8 s, and 10 s to generate Figs. 5a, 5b, and 5c, respectively. However, the snapshots in Figs. 5b and 5c computed by the fourth-order LWC and SG methods show serious numerical dispersion, whereas Fig. 5a computed by the IRK-PCM shows no visible numerical dispersion, even the spatial increment is chosen by $\Delta x = \Delta y = \Delta z = 48$ m without any additional treatments. Those comparisons demonstrate that the IRK-PCM can effectively eliminate the numerical dispersion caused by discretizing the wave equation for the coarse
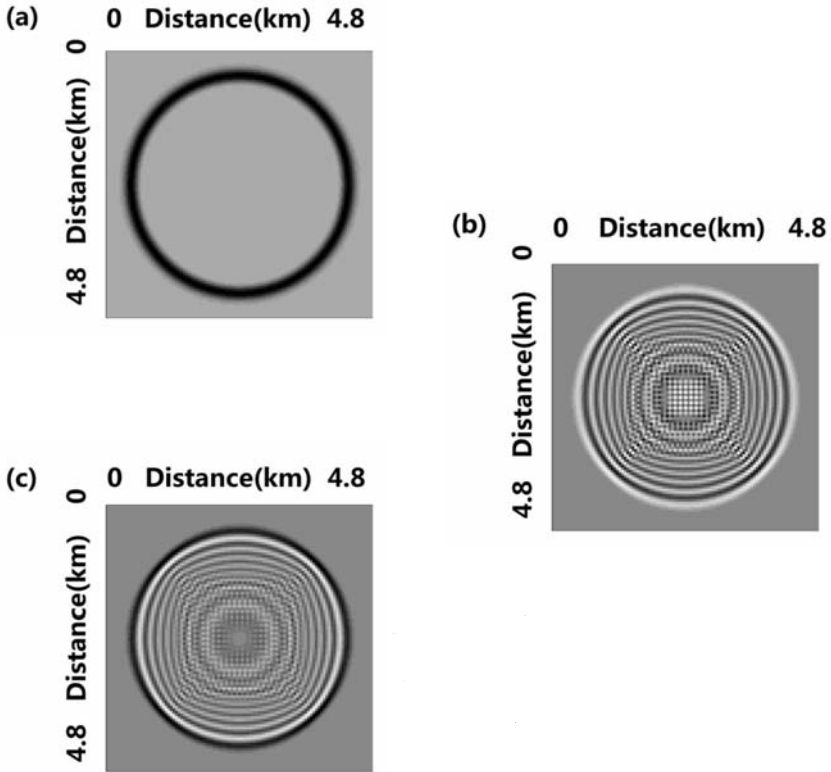
Fig. 6. Snapshots of acoustic wave fields at time 0.5 s on the coarse grid ($\Delta x = \Delta y = \Delta z = 48$ m), generated by the IRK-PCM, the fourth-order LWC, and the fourth-order SG method, respectively.
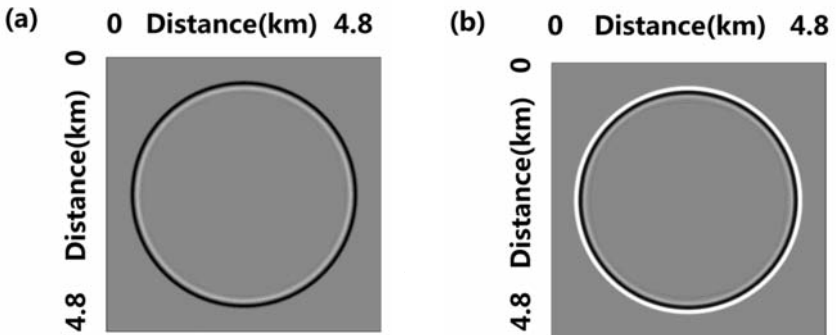

Fig. 7. Snapshots of acoustic wave fields at time 0.5 s on the fine grid ($\Delta x = \Delta y = \Delta z = 20$ m), generated by (a) the fourth-order LWC, and (b) the fourth-order SG method, respectively.

mesh case. It suggests that the IRK-PCM can improve computational efficiency when a coarse mesh is used for large scale wave-field simulations.

To further investigate the efficiency of the-IRK-PCM, Fig. 7 shows the snapshots of seismic wave fields at t = 0.5 s in the x-y plane, generated by the fourth-order LWC and SG methods, respectively, under the same Courant number but on the fine-grid step of $\Delta x = \Delta y = \Delta z = 20$ m. Figs. 6 and 7 show that the IRK-PCM can provide us an identical result on a coarse grid ($\Delta x = \Delta y = \Delta z = 48$ m) as that of the LWC and SG methods on a finer grid.

Fig. 8 shows the comparison of waveforms computed by the analytical solution (see eqs. (6.53) and (6.59), Aki and Richards, 2002) and numerical solutions calculated by the IRK-PCM for the acoustic model with $c_0 = 4$ km/s. The source wavelet has the form as (22) with a peak frequency of $f_0 = 15$ Hz. The force source and a receiver R are located at (2 km, 2 km, 2 km) and (1.4 km, 2 km, 2 km), respectively. The spatial increment and temporal step are respectively $\Delta x = \Delta y = \Delta z = 20$ m and $\Delta t = 0.005$ s. The waveforms show an excellent agreement between the analytical solution and that of the 3D IRK-PCM, which demonstrates that the IRK-PCM can provide the same accuracy as the analytic solution. For further test the accuracy of the IRK-PCM for calculating seismograms, we chose a coarser grid with $\Delta x = \Delta y = \Delta z = 60$ m, and under a peak frequency of $f_0 = 20$ Hz for the same acoustic model.
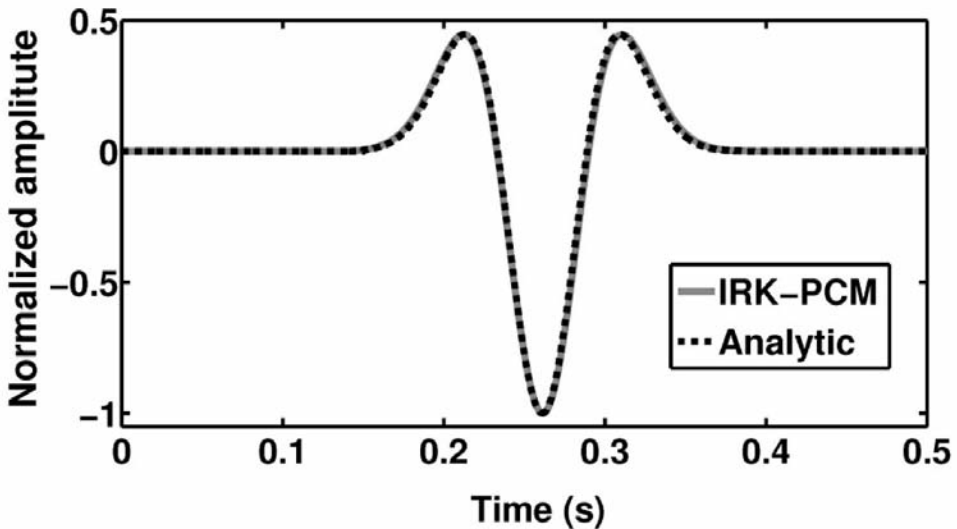

Fig. 8. Comparison of the waveforms between the analytic solution and numerical solution generated by the IRK-PCM on a fine grid with $\Delta x = \Delta y = \Delta z = 20$ m.

Fig. 9 is the waveform comparison between the analytical solution and the numerical solution, computed respectively by the IRK-PCM, the LWC, and the SG methods. We see from Fig. 9a that IRK-PCM matches the analytical solution well even under such a coarse grid, whereas other two methods suffer from numerical dispersions with the amplitudes oscillates from the analytical solution (Figs. 9b, c).

Moreover, to simulate the same region and to achieve the same good results without numerical dispersion, the IRK-PCM needs less memory and smaller computational costs. Actually, it took the IRK-PCM about 166 s to generate Fig. 6a, whereas under the same computer environment, it took the fourth-order LWC roughly 3465 s and the SG about 5142 s to generate Figs. 7a and 7b, respectively. It means that the computational speed of the IRK-PCM is about 21 times of the fourth-order LWC method, and roughly 30 times of the SG method on a fine grid to achieve the same accuracy of the IRK-PCM. Meanwhile, the required storage space for the IRK-PCM is also different from those of the fourth-order LWC and the SG method. The IRK-PCM needs 32 arrays to store $u_{i,j,k}^n$, $w_{i,j,k}^n$, $u_{i,j,k}^{n+1}$, $w_{i,j,k}^{n+1}$ and their gradients, and the number of grid points is $101 \times 101 \times 101$ on a coarse grid for generating Fig. 6a. The fourth-order LWC only needs 6 arrays to store the displacement $u_{i,j,k}^{n-1}$, $u_{i,j,k}^n$, $u_{i,j,k}^{n+1}$ and their spatial partial derivatives $(\partial^2 u/\partial x^2)_{i,j,k}^n$, $(\partial^2 u/\partial y^2)_{i,j,k}^n$, $(\partial^2 u/\partial z^2)_{i,j,k}^n$, and SG method needs 9 arrays to store the wave displacement and the stress fields at each grid point, but the number of grid points for generating Figs. 7a and 7b on the fine grid goes up to $401 \times 401 \times 401$ for the fourth-order LWC and or the SG method. It implies that the space storage of the IRK-PCM requires only roughly 8.5% of the fourth-order LWC method and about 5.7% of the SG method.

WAVE-FIELD MODELING

Two-layered acoustic model

To investigate the validity of the 3D IRK-PCM, in seismic wave field simulation we choose a two-layer acoustic medium with wave velocities 2 km/s and 4 km/s in the upper and lower layers, respectively. The number of grid points is $201 \times 201 \times 201$, the computational region is $0 < x \leq 6$ km, $0 < y \leq 6$ km, $0 < z \leq 6$ km.

The source wavelet is a $f_0 = 24$ Hz peak frequency symmetric Ricker wavelet:

$$f(t) = -5.76f_0^2[1 - 16(0.6f_0t-1)^2]\exp[-4(0.6f_0t-1)^2] \quad . \tag{23}$$

The source is located at $(x_s,y_s,z_s) = (3$ km, 3 km, 2.7 km$)$. The spatial increments are $\Delta x = \Delta y = \Delta z = 30$ m, and the time increment is $\Delta t = 0.0075$ s.
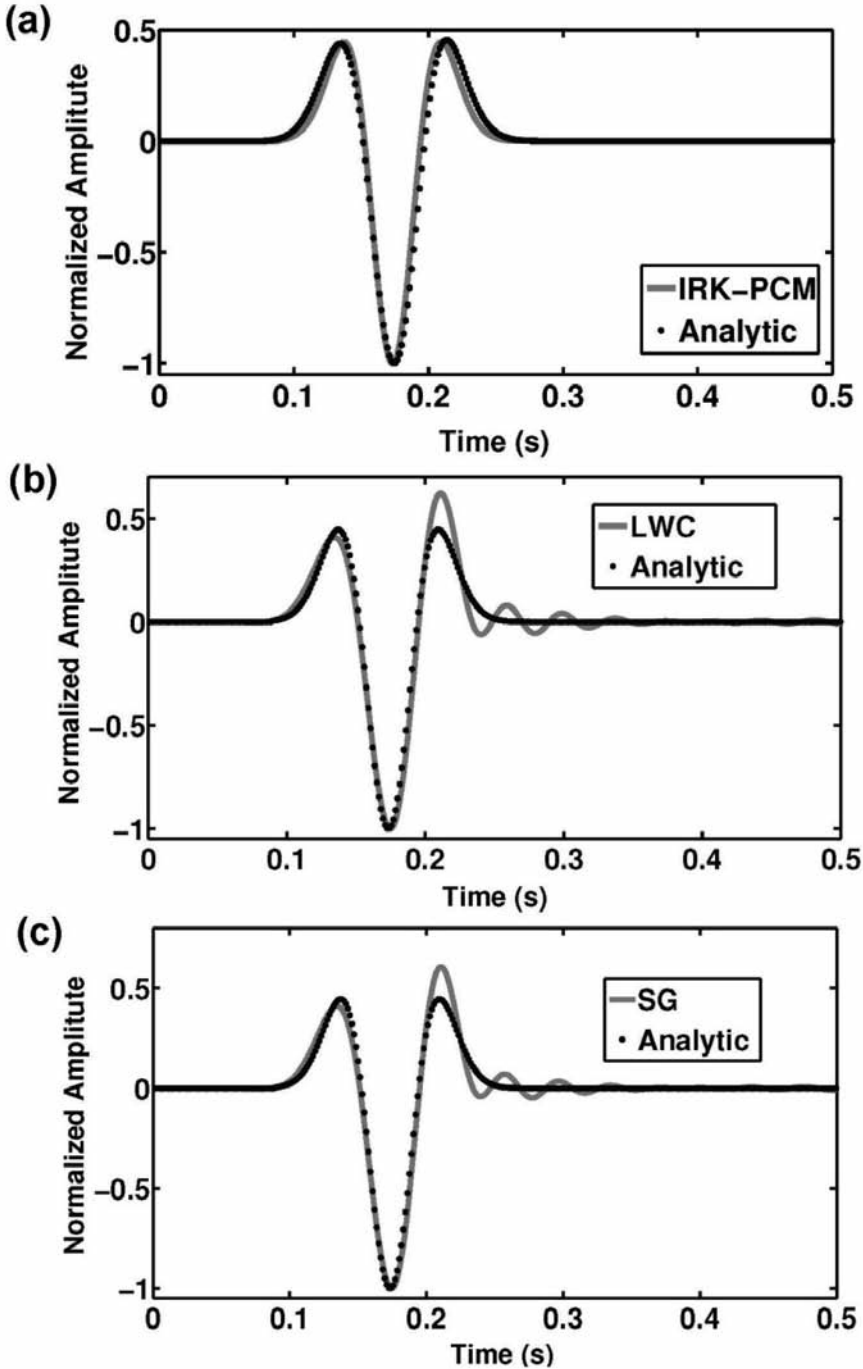
Fig. 9. Comparisons of the waveforms between the analytic solution and numerical solution generated by (a) the IRK-PCM, (b) the fourth-order LWC, and (c) the fourth-order SG, on a coarse grid with $\Delta x = \Delta y = \Delta z = 60$ m.

Fig. 10 is the wave-field snapshots at 0.9 s in the x-z plane, generated by the 3D IRK-PCM, the fourth-order LWC, the fourth-order SG, respectively. From the wave-field snapshot Fig. 10a, we can observe clearly the direct wave, the refraction wave, and the reflection of the acoustic wave from the inner interface. Also, the wave-field snapshot calculated by the IRK-PCM has almost no numerical dispersions, even if the model velocity contrast between adjacent layers is 2 times. However, the fourth LWC and SG have much serious dispersions. It took the IRK-PCM about 3.37 hours to obtain the result in Fig. 9a.

We show in Fig. 11 the two-layer acoustic waveforms recorded at 0.8 s generated by the IRK-PCM, the fourth-order LWC, the fourth-order SG, respectively. The source wavelet and peak frequency are same as Fig. 10. The spatial increment and temporal steps are respectively $\Delta x = \Delta y = \Delta z = 30$ m and $\Delta t = 0.003$ s. The receiver is at R (1.05 km,1.5 km,1.5 km), and the source is located at $(x_s, y_s, z_s) = (3$ km, 3 km, 2.7 km). It is clearly shown IRK-PCM has almost no numerical dispersions while the LWC and SG have serious dispersion on the coarse grid.
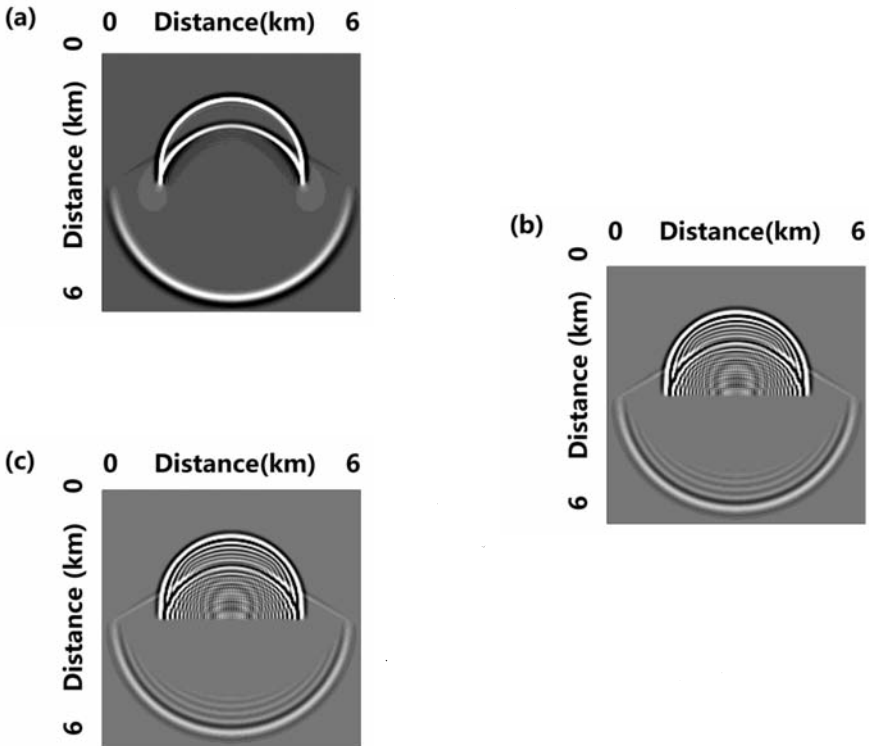

Fig. 10. Snapshots of acoustic wave-fields for a two-layer acoustic model at time 0.9 s in the x-z plane on the coarse grid ($\Delta x = \Delta y = \Delta z = 30$ m), generated by (a) the IRK-PCM, (b) the fourth-order LWC, and (c) the fourth-order SG.
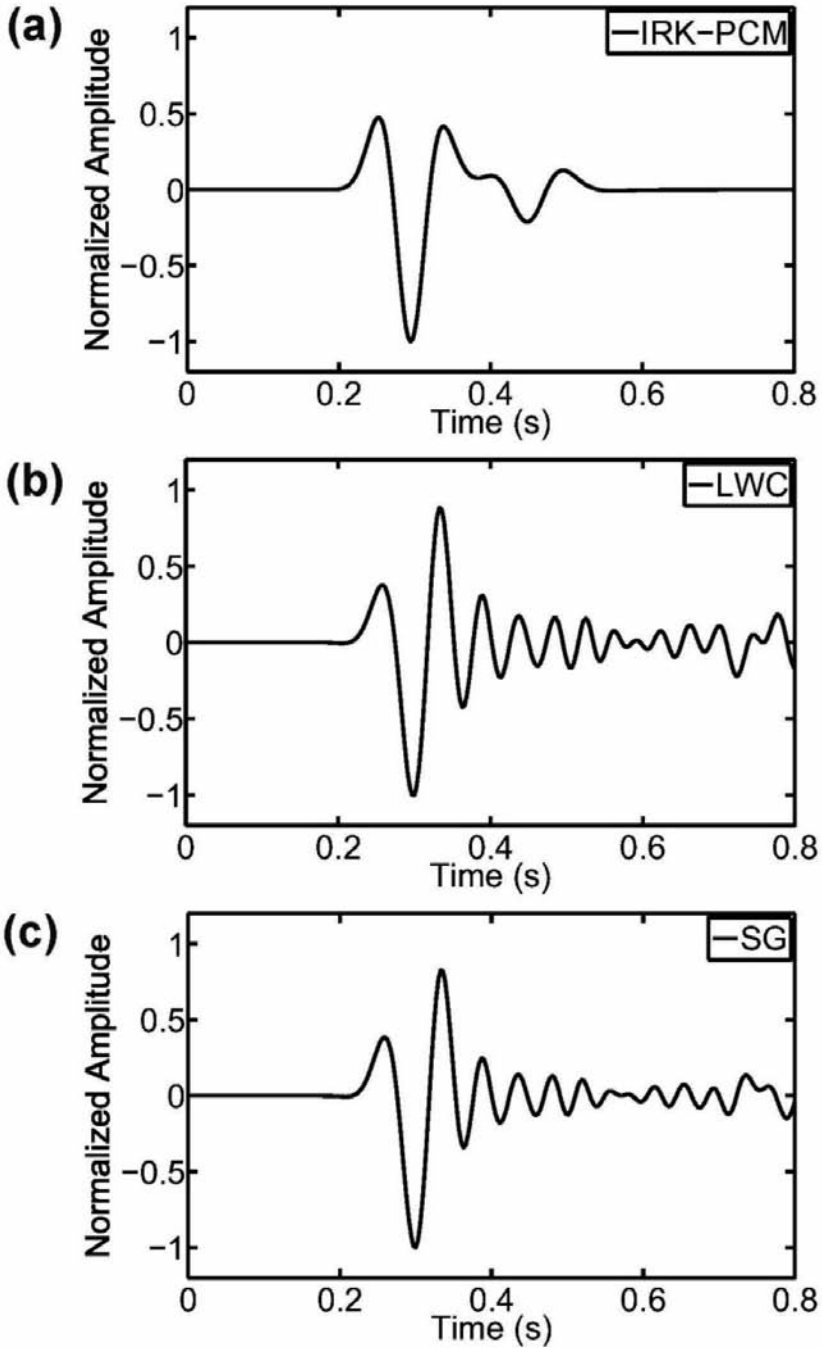
Fig. 11. The two-layer acoustic waveforms recorded at receiver R(1.05 km, 1.5 km, 1.5 km) generated on a coarse grid $\Delta x = \Delta y = \Delta z = 30$ m by (a) the IRK-PCM, (b) the fourth-order LWC, and (c) the fourth-order SG, respectively.

For practical use of the 3D IRK-PCM, we show its efficiency of acoustic wave field modeling when combined with a 2-times absorbing boundary condition (Yang et al., 2002) in Figs. 12 and 13. For comparison, Figs. 12a and 12b respectively show the snapshots of wave field in x-y plane at 0.22 s for an acoustic model with velocity of 4 km/s without and with absorbing boundary condition. We see that the reflected waves at the four boundaries are absorbed and we get a perfect wave-front information of the acoustic wave by using the absorbing boundary condition (Fig. 12b). Similarly, we show synthetic seismograms in Fig. 13 on the surface for a 2-layered acoustic model (Jarchow et al., 1994) without (Fig. 13a) and with (Fig. 13b) the 2-times absorbing
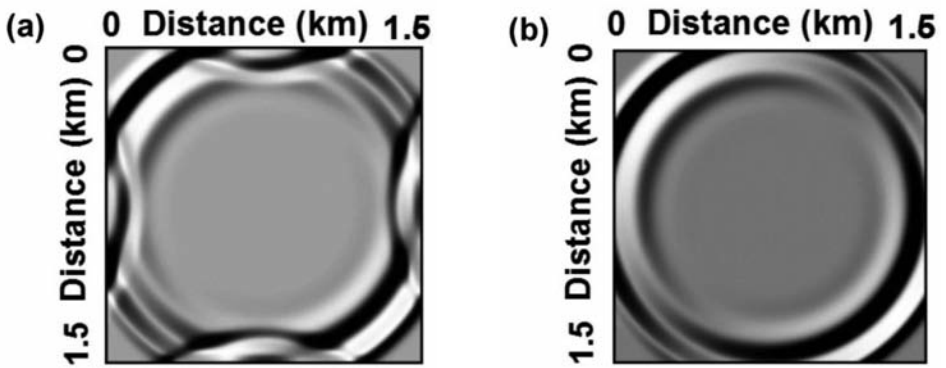
Fig. 12. Snapshots of wave field in the x-y plane at 0.22 s for an acoustic model computed by the IRK-PCM, (a) without and (b) with the 2-times absorbing boundary condition, respectively.
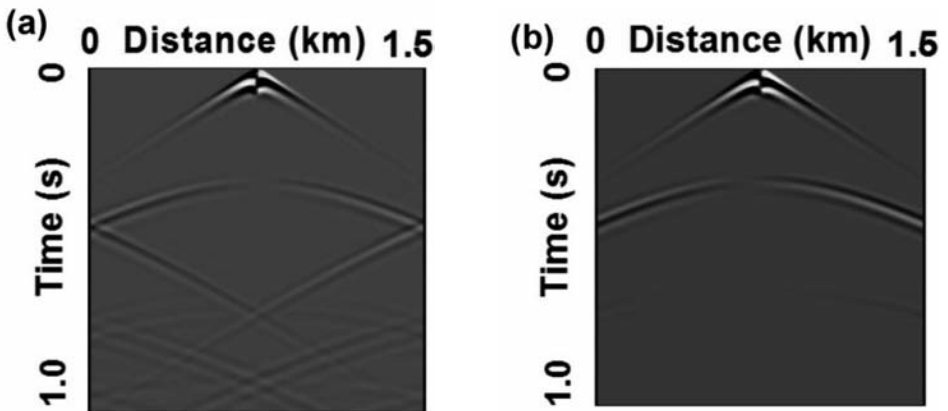
Fig. 13. Synthetic seismograms on the surface for a 2-layered acoustic model computed by the IRK-PCM, (a) without and (b) with the 2-times absorbing boundary condition, respectively.

boundary condition, respectively. The acoustic velocity in the upper layer is 2 km/s, and in the lower layer is 4 km/s. Without the absorbing boundary condition, various reflected waves are observed in Fig. 13a which will misguide us interpreting the structure of the acoustic model investigated. However, we recover the wave field information in synthetic seismograms with the direct wave and the easily picked reflected waves (Fig. 13b) by introducing the absorbing boundary condition (Yang et al., 2002).
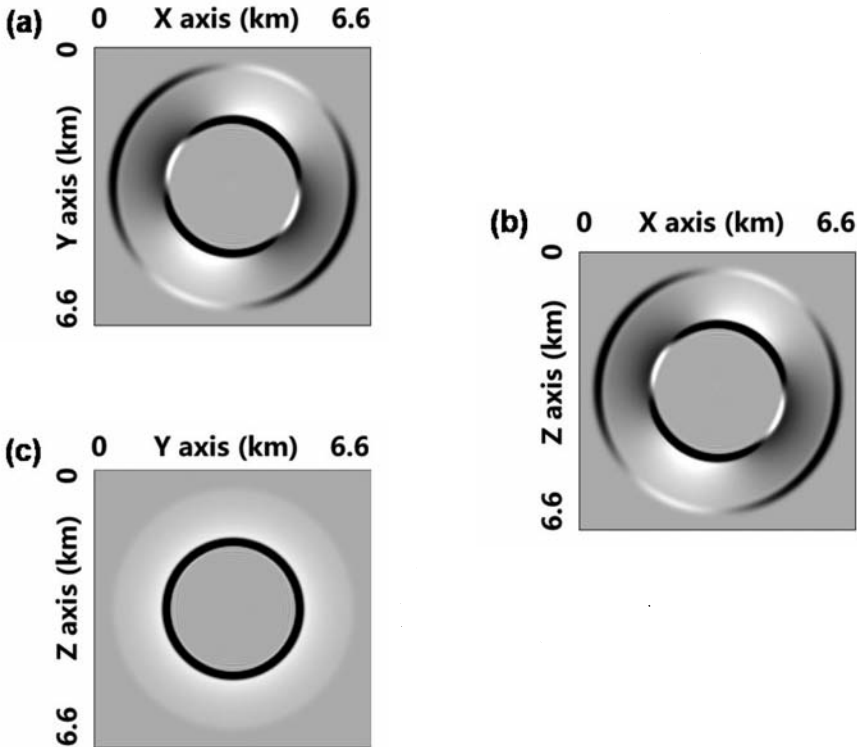

Fig. 14. Snapshots of seismic wave-fields at time 1.2 s for the displacement component u_1 in (a) the x-y plane, (b) the x-z plane, and (c) the y-z plane, for the isotropic elastic medium generated by the IRK-PCM on a coarse grid $\Delta x = \Delta y = \Delta z = 33$ m.

Isotropic elastic model

To further investigate the validity of the IRK-PCM for the 3D isotropic elastic case, we choose the elastic constants by $\lambda = 4.75$ GPa, $\mu = 3.75$ GPa, and the density $\rho = 2.1$ g/cm^3. The spatial and time increments are respectively $\Delta x = \Delta y = \Delta z = 33$ m and $\Delta t = 0.137 \times 10^{-3}$ s, and the number of grid points is $201 \times 201 \times 201$. The force source is the same as those used in the

acoustic experiments previously with a peak frequency of f_0 15 Hz. Fig. 14 shows the wave-field snapshots of the displacement component u_1 at time 1.2 s on a coarse grid ($\Delta x = \Delta y = \Delta z = 33$ m) generated by the IRK-PCM, in the x-y (Fig. 14a), the x-z (Fig. 14b), and the y-z (Fig. 14c) planes, respectively. In Figs. 14a and 14b, the snapshots in the x-y and the x-z planes show very clear wave-fronts of the P- and SV-waves. The snapshot in the y-z plane (Fig. 14c) shows clear wave-front of the SH-wave and very weak wave-front of wave. The same waves can be found from the wave-field snapshots of u_2 and u_3 components, which are omitted here. It took about 13.45 hours to generate the results in Fig. 14 which was performed on an Intel(R) Xeon(R) CPU with 2.60 GHz and 64 GB memory.

Fig. 15 shows the waveforms computed by the 3D IRK-PCM in an elastic isotropic medium, where the peak frequencies are respectively 50 Hz (Fig. 15a), 60 Hz (Fig. 15b), and 70 Hz (Fig. 15c). The elastic constants are $\lambda = 4.11$ GPa, $\mu = 7.74$ GPa, and the density $\rho = 1.6$ g/cm^3. The spatial increment is chosen by $\Delta x = \Delta y = \Delta z = 10$ m. In Fig. 15, we see clear waveforms of P- and S-waves without visible numerical dispersions even when the peak frequency is up to 70 Hz, illustrating the effectiveness of IRK-PCM in wavefield simulation at high frequency bands.
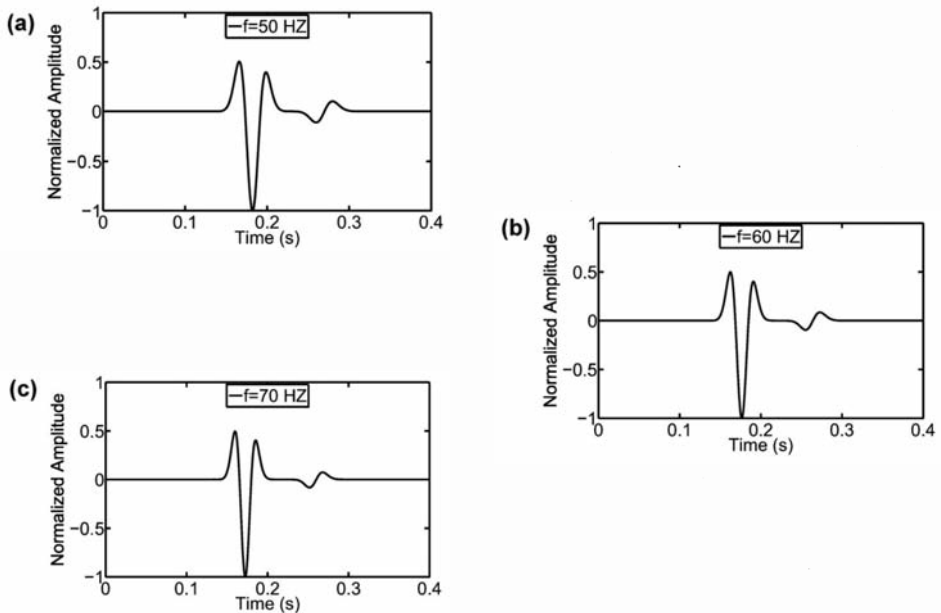

Fig. 15. Waveform records at a receiver R(0.7 km, 0.7 km, 0.7 km) for the displacement component at different high peak frequencies (a) 50 Hz, (b) 60 Hz, and (c) 70 Hz for the isotropic elastic medium generated by the IRK-PCM.

VTI Model

In this subsection, we choose the transversely isotropic model with a vertical symmetry axis (VTI) for which the medium parameters are listed in Table 2. The spatial and time increments are $\Delta x = \Delta y = \Delta z = 30$ m and $\Delta t = 0.8 \times 10^{-3}$ s, respectively. The number of grid points is $201 \times 201 \times 201$, and the computation domain is $0 < x \le 6$ km, $0 < y \le 6$ km and $0 < z \le 6$ km. The source and the peak frequency are the same as those used in the isotropic elastic model.

Table 2. Medium parameters used in the VTI model.

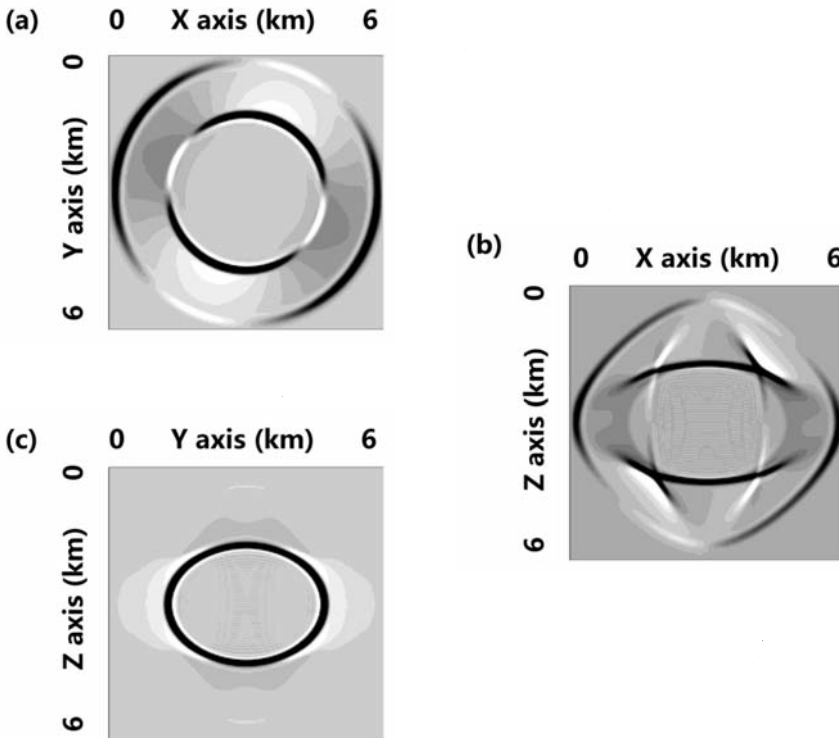| c_{11} (GPa)	c_{12} (GPa)	c_{11} (GPa)	c_{12} (GPa)	c_{11} (GPa)	c_{12} (GPa)	ρ_s g/cm³
20	6	4.5	17.5	4	7	1.8

Fig. 16. Snapshots of seismic wave-fields at time 0.88 s for the displacement component u_1 in the VTI medium on a coarse grid $\Delta x = \Delta y = \Delta z = 30$ m, generated by the IRK-PCM.

The wave-field snapshots for three components u_1, u_2 and u_3 at time 0.88 s are given in Figs. 16, 17, and 18. Fig. 16 respectively presents the snapshots of the u_1 component in the x-y, the x-z, and the y-z planes. Figs. 17 and 18 show the snapshots of displacement components u_2 and u_3 in three coordinate planes. The wave-field snapshots in the x-y plane (transverse plane) for the three displacement components which are shown in Figs. 16a, 17a, and 18a, illustrate that the wave-fronts of P- and S-waves are circles in the VTI medium. Whereas other snapshots in Figs. 16, 17, and 18 show that the wave-fronts of the quasi-P (qP), quasi-SV (qSV) waves and quasi-SH (qSH) waves are elliptical, implies the propagation velocity of these waves have a directional dependence. The qSV wave-fronts can have cusps and triplications depending on the value of c_{13} (Faria and Stoffa, 1994). Triplications can be observed in the horizontal component qSV wavefronts in the x-z plane for the u_1 component (Fig. 16b), in the y-z plane for the u_2 component (Fig. 17c), and in the vertical component qSV wavefronts presented in Figs. 18b and 18c.
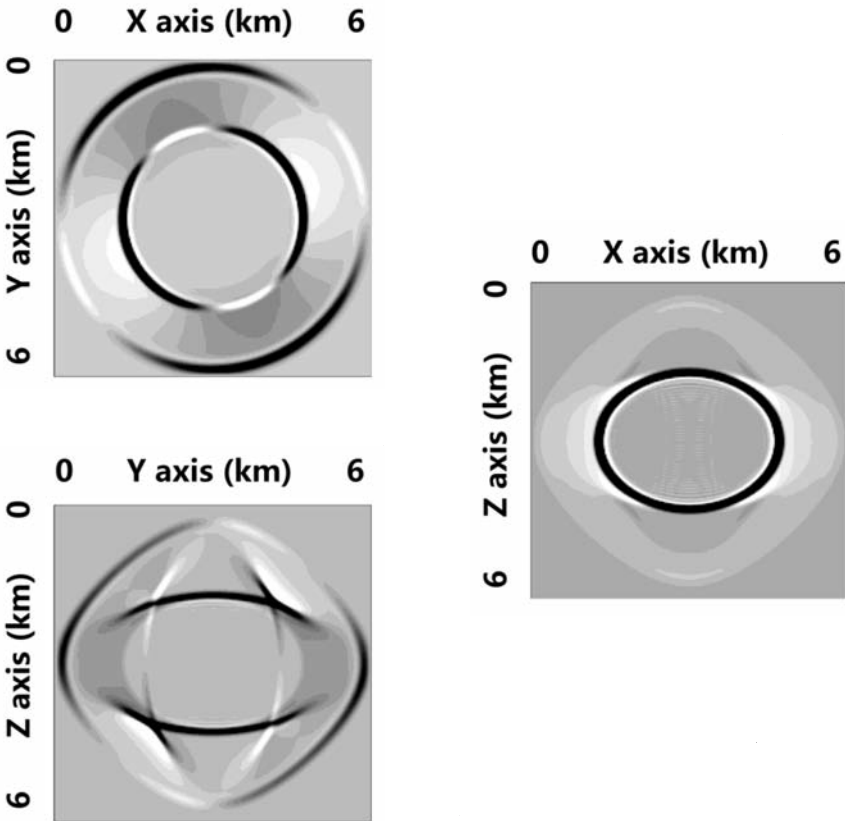

Fig. 17. Snapshots of seismic wave-fields at time 0.88 s for the displacement component u_2 in the VTI medium on a coarse grid $\Delta x = \Delta y = \Delta z = 30$ m, generated by the IRK-PCM.

By using the Christoffel equation, the velocities of quasi SV-wave and SH-wave can be expressed by elastic parameters of the medium and the angle θ between the axis of symmetry and the wave propagation direction, i.e., $V_{qSV}(\theta) = \sqrt{\{[C_{11}\sin^2(\theta) + C_{33}\cos^2(\theta) + C_{44} - \sqrt{M(\theta)}]/2\rho\}}$, $V_{qSH}(\theta) = \sqrt{\{[C_{66}\sin^2(\theta) + C_{44}\cos^2(\theta)]/\rho\}}$, $M(\theta) = [(C_{11}-C_{44})\sin^2(\theta) - (C_{33}-C_{44})\cos^2(\theta)]^2 + (C_{13}+C_{44})^2\sin^2(2\theta)$, (Mavko et al., 2003). It means that the arrival time difference between qSH and qSV waves, namely the shear-wave splitting phenomenon, depends mainly on elastic parameter C_{33}. By choosing an approximate value of C_{33}, we observe in the VTI medium the shear-wave splitting phenomenon through comparing Figs. 16c and 17b with Figs. 16b and 17c, 18b and 18c. It took the IRK-PCM about 10.68 hours to generate Figs. 16, 17 and 18 on an Intel(R) Xeon(R) CPU with 2.60 GHz and 64 GB memory.
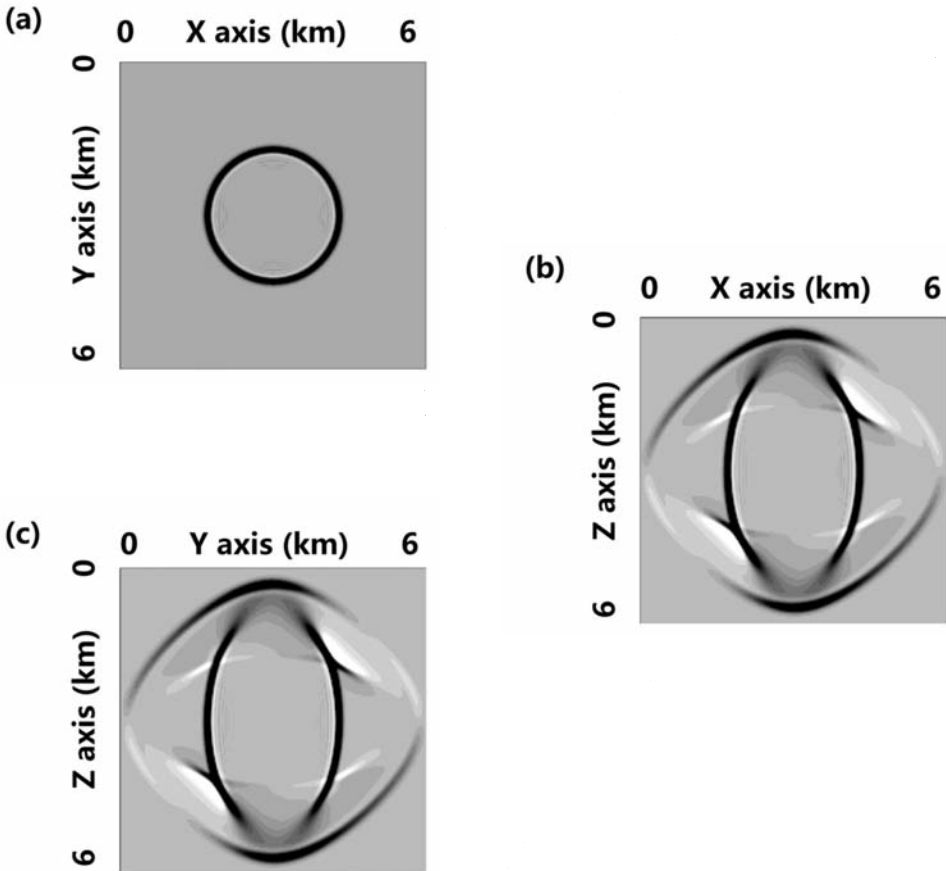

Fig. 18. Snapshots of seismic wave-fields at time 0.88 s for the displacement component u_3 in the VTI medium on a coarse grid $\Delta x = \Delta y = \Delta z = 30$ m, generated by the IRK-PCM.

CONCLUSION AND DISCUSSION

In this article, we propose the 3D predictor-corrector algorithm (IRK-PCM) based on the implicit Runge-Kutta method, and apply it to solve the acoustic- and elastic- wave eqs.. We first transform the wave equation to a system of ordinary differential eqs., and then use the predictor-corrector method based on an implicit Runge-Kutta method to solve the ODEs. In detail, we first transform the original wave eq. (2) into eq. (7). And then we use the interpolation approximations (A-1)-(A-5) to approximate the high-order spatial derivatives on the right-hand side of eq. (7), so that it is converted into a system of semi-discrete ordinary differential eqs. (ODEs). Finally, we solve the semi-discrete eq. (7) using the IRK-PCM for the temporal discretization, which is actually an extension of the 2D IRK-PCM (Wang et al., 2012).

The theoretical error analysis shows that the IRK-PCM has fourth-order accuracy in space and second-order accuracy in time, which is confirmed by the numerical experiments for different cases. Using the Fourier analysis method (Richtmyer and Morton, 1967), we get the stability condition of the IRK-PCM for solving the 3D acoustic equation [see eqs. (18) or (20)]. Theoretical dispersion analysis illustrates that the IRK-PCM can effectively suppress the numerical dispersion even when the grid sampling per wavelength is about 3 (numerical error is within 2%) (Figs. 4 and 5). Numerical simulations of acoustic and elastic media in the wave-field modeling section, illustrate that the IRK-PCM provides us accurate wave field information without numerical dispersion (through snapshots and seismograms), even in the situation of coarse grid or at high frequency bands, or geological models with large velocity contrasts.

It appears that the IRK-PCM costs more CPU time per iteration than the fourth-order LWC and staggered-grid methods, but it yields less numerical dispersion than the fourth-order LWC and SG methods. Therefore, we can reduce computational time and space storage through choosing larger spatial or time increments for the IRK-PCM, to achieve the same accuracy as those of the LWC and SG methods on a fine grid with smaller time steps. Thus, as is confirmed in the computational efficiency section, to achieve the same accurate snapshots without numerical dispersions, the computational speed of the IRK-PCM on a coarse grid is about 25 times of the fourth-order LWC and 30 times of the fourth-order SG on a fine grid, and the space storage of the IRK-PCM requires only roughly 8.5% of the fourth-order LWC and 5.7% of the fourth-order SG. For its efficiency of suppressing numerical dispersion even when about 3 points per wavelength are used, we conclude that the 3D IRK-PCM provides us an useful tool for the 3D large-scale isotropic and anisotropic wave-field modeling, reverse time migration and full waveform inversion.

ACKNOWLEDGEMENTS

REFERENCES

Aki, K. and Richards, P.G., 1980. Quantitative Seismology. W.H. Freeman and Co., San Francisco.

Alford, R.M., Kelly, K.R. and Boore, D.M., 1974. Accuracy of finite-difference modeling of the acoustic wave equation. Geophysics, 39: 834-842.

Chen, S., Yang, D.H. and Deng, X.Y., 2009. A weighted Runge-Kutta method with weak numerical dispersion for solving wave equations. Commun. Comput. Phys., 7: 1027-1048.

Ciarlet, P.G., 1978. The Finite Element Method for Elliptic Problems. North-Holland Publishing Co., Amsterdam.

Dablain, M.A., 1986. The application of high-order differencing to the scalar wave equation. Geophysics, 51: 54-66.

Eriksson, K. and Johnson, C., 1991. Adaptive finite element methods for parabolic problems I: A linear model problem. SIAM J. Numer. Anal., 28: 43-77.

Faria, E.L., and Stoffa, P.L., 1994. Finite-difference modeling in transversely isotropic media. Geophysics. 59: 282-289.

Fei, T. and Larner, K., 1995. Elimination of numerical dispersion in finite-difference modeling and migration by flux-corrected transport. Geophysics, 60: 1830-1842.

Fornberg, B., 1990. High-order finite differences and pseudo-spectral method on staggered grids. SIAM J. Numer. Anal. 27: 904-918.

Gottlied, D. and Orzag, S., 1977. Numerical Analysis of Spectral Methods: Theory and Applications. SIAM, Philadelphia.

Guan, Z. and Lu, J.F., 2006. Numerical Methods. Tsinghua University Press, Beijing.

Hairer, E., Nørsett, S.P. and Wanner, G., 1993. Solving Ordinary Differential Equations. I: Nonstiff Problems. Springer-Verlag, Berlin, Heidelberg.

Igel, H., Mora, P. and Riollet, B., 1995. Anisotropic wave propagation through finite-difference grids. Geophysics, 60: 1203-1216.

Jarchow, C.M., Catchings, R.D. and Lutter, W.J., 1994. Large-explosive source, wide-recording aperture, seismic profiling on the Columbia Plateau, Washington. Geophysics, 59: 259-271.

Johnson, C., 1990. Adaptive finite element methods for diffusion and convection problems. Comput. Methods Appl. Mech. Engin., 82: 301-322.

Kelly, K., Ward, R., Treitel, S. and Alford, R., 1976. Synthetic seismograms: a finite-difference approach. Geophysics, 41: 2-27.

Komatitsch, D. and Vilotte, J.P., 1998. The Spectral Element method: an efficient tool to simulate the seismic response of 2D and 3D geological structures. Bull. Seismol. Soc. Am., 88: 368-392.

Komatitsch, D., Barnes, C. and Tromp, J., 2000. Simulation of anisotropic wave propagation based upon a spectral-element method. Geophysics, 65: 1251-1260.

Konddoh, Y., Hosaka, Y. and Ishii, K., 1994. Kernel optimum nearly analytical discretization algorithm applied to parabolic and hyperbolic equations. Comput. Math. Appl., 27: 59-90.

Lax, P.D. and Wendroff, B., 1964. Difference schemes for hyperbolic equations with high order of accuracy. Commun. Pure Appl. Math., 172: 381-398.

Ma, X., Yang, D.H. and Liu, F., 2011. A nearly analytic symplectically partitioned Runge-Kutta method for 2D seismic wave equations. Geophys. J. Internat., 187: 480-496.

Ma, X., Yang, D.H., Song, G.J. and Wang, M.X., 2014. A low-dispersive symplectic partitioned

Runge-Kutta method for solving seismic wave equations - I. Scheme and theoretical analysis. Bull. Seismol. Soc. Am., 104 (5) (doi: 10.1785/0120120210, in press).

Mavko, G., Mukerji, T. and Dvorkin, J., 2003. The Rock Physics Handbook, 2nd ed. Cambridge Univ. Press, Cambridge.

Mocoz, P., Kristek, J. and Halada, L., 2000. 3D fourth-order staggered-grid finite-difference schemes: Stability and grid dispersion, Bull. Seism. Soc. Am., 90: 587-603.

Richtmyer, R.D. and Morton, K.W., 1967. Difference Methods for Initial Value Problems. Interscience, New York.

Sei, A. and Symes, W., 1994. Dispersion analysis of numerical wave propagation and its computational consequences. J. Sci. Comput., 10: 1-27.

Solin, P., Segeth, K. and Dolezel, I., 2003. Higher-Order Finite Element Methods. Chapman & Hall/CRC Press, London.

Takeuchi, N. and Geller, R.J., 2000. Optimally accurate second order time-domain finite-difference scheme for computing synthetic seismograms in 2-D and 3-D media. Phys. Earth Planet. Inter., 119: 99-131.

Turner, M.J., Clough, R.W., Martin, H.C. and Topp, L.J., 1956. Stiffness and deflection analysis of complex structures. J. Aeronaut. Sci., 23: 805-823.

Virieux, J., 1986. P-SV wave propagation in heterogeneous media: Velocity-stress finite-difference method. Geophysics, 51: 889-901.

Wang, N., Yang, D.H. and Liu, F.Q., 2012. Weak dispersion wave-field simulations: a predictor-corrector algorithm for solving acoustic and elastic wave eqs., J. Seismic Explor., 21: 125-152.

Wang, S. Q., Yang, D.H. and Yang, K.D., 2002. Compact finite difference scheme for elastic equations. J. Tsinghua Univ. (Sci. & Tech), 42: 1128-1131 (in Chinese).

Whiteman, J.R., 1975. A Bibliography for Finite Elements. Academic Press Inc., New York.

Yang, D.H. and Wang, L., 2010. A split-step algorithm for effectively suppressing the numerical dispersion for 3D seismic propagation modeling. Bull. Seismol. Soc. Am., 100: 1470-1484.

Yang, D.H., Liu, E. and Zhang, Z.J., 2008. Evaluation of the u-W finite element method in anisotropic porous media. J. Seismic Explor., 17: 273-299.

Yang, D.H., Liu, E.R., Zhang, Z.J. and Teng, J.W., 2002. Finite-difference modeling in two-dimensional anisotropic media using a flux-corrected transport technique. Geophys. J. Internat., 148: 320-328.

Yang, D.H., Song, G.J. and Zhang, J.H., 2010. A modified NAD algorithm with minimum numerical dispersion for simulation of anisotropic wave propagation. J. Seismic Explor., 19: 21-42.

Yang, D.H., Song, G.J. and Lu, M., 2007. Optimally accurate nearly analytic discrete scheme for wave-field simulation in 3D anisotropic media. Bull. Seismol. Soc. Am., 97: 1557-1569.

Yang, D.H., Song, G.J., Chen, S. and Hou, B.Y., 2007. An improved nearly analytical discrete method: an efficient tool to simulate the seismic response of 2D porous structures. J. Geophys. Engin., 4: 40-52.

Yang, D.H., Teng, J.W., Zhang, Z.J. and Liu, E.R., 2003. A nearly-analytic discrete method for acoustic and elastic wave equations in anisotropic media. Bull. Seismol. Soc. Am., 93: 882-890.

Yang, D.H., Wang, M.X. and Ma, X., 2014. Symplectic stereomodelling method for solving elastic wave equations in porous media. Geophys. J. Internat., 196: 560-579.

Yang, D.H., Wang, N. and Liu, E., 2012. A strong stability-preserving predictor corrector method for the simulation of elastic wave propagation in anisotropic media. Commun. Comput. Phys., 12: 1006-1032.

Zahradnik, J., Moczo, P. and Hron, T., 1993. Testing four elastic finite-difference schemes for behavior at discontinuities. Bull. Seismol. Soc. Am., 83: 107-129.

Zhang, Z.J., Wang, G.J. and Harris, M.J., 1999. Multi-component wave-field simulation in viscous extensively dilatancy anisotropic media. Phys. Earth Planet. Inter., 114: 25-38.

Zheng, H.S., Zhang, Z.J. and Liu, E.R., 2006. Non-linear seismic wave propagation in anisotropic media using the flux-corrected transport technique. Geophys. J. Int., 165: 943-956.

APPENDIX A

APPROXIMATIONS OF HIGH-ORDER DERIVATIVES

For the 2D case, we have shown the formulae to calculate the second-order and third-order spatial derivatives, which involved in the algorithm IRK-PCM when solving the acoustic and elastic wave eqs. (Wang et al., 2012). These formulae are based on the local interpolation methods in which the nearly-analytic discrete operators are introduced, and can be easily extended to the 3D case (Konddoh et al., 1994; Yang et al., 2003, 2007; Yang and Wang, 2010). In the local interpolation method, to calculate the spatial derivatives at each grid point, we introduce spatial operators that involve only three grid points that adjacent to it in each of the three directions.

Speaking in detail, when we use the explicit IRK-PCM to compute the values of U at time t_{n+1} in synthetic seismograms, we first need to compute the high-order space derivatives included in the general eq. (7) or the detailed eqs. (8-15) for the algorithm IRK-PCM. Following the local interpolation theory and introducing the corresponding displacement operators (Yang et al., 2007; Yang and Wang, 2010), we present here the approximation formulae for the second-order spatial derivatives in 3D IRK-PCM as

$$(\partial^2 V/\partial g^2)_{i,j,k}^n = [2/(\Delta g)^2]\delta_g^2 V_{i,j,k}^n$$

$$- (1/2\Delta g)(E_g^1 - E_g^{-1})(\partial V/\partial g)_{i,j,k}^n \quad , \quad g = x,y,z, \tag{A-1}$$

$$(\partial^2 V/\partial g \partial e)_{i,j,k}^n = (1/2\Delta g)(E_g^1 - E_g^{-1})(\partial V/\partial g)_{i,j,k}^n$$

$$+ (1/4\Delta g \Delta e)(E_g^1 E_e^1 + E_g^{-1}E_e^{-1} - E_g^1 E_e^{-1} - E_g^{-1}E_e^1)V_{i,j,k}^n \quad , \tag{A-2}$$

corresponding to three cases $g = x$, $e = y$, $g = y$, $e = z$, and $g = z$, $e = x$, and conditions $(\partial^2 V/\partial g \partial e)_{i,j,k}^n = (\partial^2 V/\partial e \partial g)_{i,j,k}^n$ are constrained for different pairs of g and e.

The third-order spatial derivatives in IRK-PCM are given as follows

$$(\partial^3 V/\partial g^3)_{i,j,k}^n = [15/2(\Delta g)^3](E_g^1 - E_g^{-1})V_{i,j,k}^n$$

$$-[3/2(\Delta g)^2](E_g^1 + 8I - E_g^{-1})V_{i,j,k}^n \quad , \quad g = x,y,z, \tag{A-3}$$

$$(\partial^3 V/\partial g^2 \partial e)_{i,j,k}^n = (1/2\Delta g \Delta e)(-E_g^1 E_e^1 - E_g^{-1}E_e^{-1}E_g^1 + E_g^{-1} - 2\delta_e^2)(\partial V/\partial g)_{i,j,k}^n$$

$$+ (1/\Delta g)^2\delta_g^2(\partial V/\partial e)_{i,j,k}^n + [1/4(\Delta g)^2\Delta e](5E_g^1 E_e^1 - 5E_g^{-1}E_e^{-1}$$

$$+ E_g^1 E_e^{-1} - E_g^{-1}E_e^1 - 6E_g^1 + 6E_g^{-1} - 4E_e^1 + 4E_e^{-1})V_{i,j,k}^n \quad , \tag{A-4}$$

where g,e $=$ x,y,z, and g $\neq$ e, and conditions $(\partial^3 V/\partial g^2 \partial e)^n_{i,j,k} = (\partial^3 V/\partial e \partial g^2)^n_{i,j,k}$ are constrained for different pairs of g and e, and

$$
\begin{aligned}
(\partial^3 V/\partial x \partial y \partial z)^n_{i,j,k} = {} & (1/4\Delta y \Delta z)(E^1_y E^1_z + E^{-1}_y E^{-1}_z - E^1_y E^{-1}_z - E^{-1}_y E^1_z)(\partial V/\partial x)^n_{i,j,k} \\
& + (1/4\Delta x \Delta z)(E^1_x E^1_z + E^{-1}_x E^{-1}_z - E^1_x E^{-1}_z - E^{-1}_x E^1_z)(\partial V/\partial y)^n_{i,j,k} \\
& + (1/4\Delta x \Delta y)(E^1_x E^1_y + E^{-1}_x E^{-1}_y - E^1_x E^{-1}_y - E^{-1}_x E^1_y)(\partial V/\partial z)^n_{i,j,k} \\
& - (1/4\Delta x \Delta y \Delta z)(E^1_x E^1_y E^1_z + E^{-1}_x E^{-1}_y E^{-1}_z + E^{-1}_x E^{-1}_y E^1_z - E^1_x E^1_y E^{-1}_z \\
& + E^{-1}_x E^1_y E^{-1}_z - E^1_x E^{-1}_y E^1_z - E^1_x E^{-1}_y E^{-1}_z - E^{-1}_x E^1_y E^1_z) V^n_{i,j,k} \quad . \quad (A\text{-}5)
\end{aligned}
$$

The definitions of spatial operators involved in eqs. (A1)-(A5) are intuitive. For example, when g $=$ z, we have $\Delta g = \Delta z$ indicates the spatial increment in the z-direction, $\delta^2_g = \delta^2_z V^n_{i,j,k} = V^n_{i,j,k+1} - 2V^n_{i,j,k} + V^n_{i,j,k-1}$, and $E^1_g = E^1_z = V^n_{i,j,k+1}$, $E^{-1}_g = E^{-1}_z = V^n_{i,j,k-1}$, which are related to spatial operations on the z-direction. Other cases of g $=$ x correspond to operators δ^2_x, E^1_x, and E^{-1}_x on the x-direction, and g $=$ y corresponds to operators δ^2_y, E^1_y, and E^{-1}_y on the y-direction can be defined similarly.

APPENDIX B

DERIVATION OF THE STABILITY CRITERIA

For the 3D homogenous case, the stability condition of the IRK-PCM can be also easily extended from the 2D case (Wang et al., 2012). We consider the harmonic solution of eq. (8) under the condition of $\Delta x = \Delta y = \Delta z = h$, and substitute the following solution

$$
\bar{V}^n_{l,m,q} = \begin{pmatrix} \bar{V} \\ \partial_x \bar{V} \\ \partial_y \bar{V} \\ \partial_z \bar{V} \end{pmatrix}^n \exp[i(k_1 lh + k_2 mh + k_3 qh)] \quad , \tag{B-1}
$$

into eq. (8) together with relations (A-1)-(A-5), we can obtain the following eq.

$$
\bar{V}^{n+1}_{l,m,q} = G\bar{V}^{n+1}_{l,m,q} \quad , \tag{B-2}
$$

where G is the amplification matrix.

Apply the same stability criteria $\rho(G^* \cdot G) \leq 1$ as that in the 2D case where G^* the conjugate transpose matrix of G and $\rho(G^* \cdot G)$ the spectral radius of matrix (Yang et al., 2009; Wang et al., 2012), we derive in the following the stability conditions of the IRK-PCM for the 3D homogenous case

$$\alpha \leq \alpha_{max} \leq 0.505 \ , \tag{B-3}$$

or

$$\Delta t \leq \alpha_{max}(h/c_0) \approx 0.505(h/c_0) \ . \tag{B-4}$$

where $\alpha c_0 \Delta t/h$ denotes the Courant number, α_{max} denotes the maximum Courant number that keeps the IRK-PCM computational stable, and c_0 the acoustic velocity for the homogenous case. For the heterogeneous case, we choose c_0 as the maximum wave velocity of the medium.

APPENDIX C

DERIVATION OF THE NUMERICAL DISPERSION RELATION

Following the dispersion analysis methods presented in Dablain (1986) and Wang et al. (2012), we consider the harmonic solution of eq. (8) and substitute the below solution for the 3D homogeneous case under the condition of $\Delta x = \Delta y = \Delta z = h$

$$\bar{V}^n_{l,m,q} = \begin{pmatrix} \bar{V} \\ \partial_x \bar{V}_0 \\ \partial_y \bar{V}_0 \\ \partial_z \bar{V}_0 \end{pmatrix} \exp[i(-\omega_{num}n\Delta t + k_1 lh + k_2 mh + k_3 qh)] \ , \tag{C-1}$$

into eq. (8) together with relations (A1)-(A5), we can obtain the following dispersion equation

$$\text{Det}(M) = 0 \ , \tag{C-2}$$

where is the time step increment, ω_{num} is the numerical angular frequency, k_1, k_2 and k_3 are respectively the three components of the wave number vector $\mathbf{k} = (k_1, k_2, k_3)$ in x-axis, y-axis and z-axis directions. For convenience, we introduce the plane-wave propagation angle with respect to the x-axis as δ_1 and to the z-axis as δ_2, and define the L_2 norm as $|\mathbf{k}| = (k_1^2, k_2^2, k_3^2)^{\frac{1}{2}}$, then k_1, k_2 and k_3 can be substituted in eq. (C-2) as $k_1 = |\mathbf{k}|\sin\delta_2\cos\delta_1$, $k_2 = |\mathbf{k}|\sin\delta_2\sin\delta_1$, $k_3 = |\mathbf{k}|\cos\delta_2$ ($0 \leq \delta_1 < 2\pi$, $0 \leq \delta_2 < \pi$), respectively. Due to the complexity of elements of the matrix M, we omit its detailed expressions here.

From the dispersion relation (C-2), we can obtain the ratio of the numerical velocity c_{num} to the phase velocity c_0 as follows

$$R = c_{num}/c_0 = \omega_{num}\Delta t/\alpha\theta = \gamma/\alpha\theta \ , \tag{C-3}$$

where α is the Courant number, $\gamma = \omega_{num}\Delta t$, and $\theta = |\mathbf{k}|h$ satisfies the dispersion eq. (C-2). In some work, by defining the spatial sampling ratio (Moczo et al., 2000), we further have $\theta = |\mathbf{k}|h = 2\pi s$.